Tensile strength and fracture of cemented granular aggregates

Rafik Affes, Jean-Yves Delenne, Yann Monerie, Farhang Radjai, Vincent Topin

▶ **To cite this version:**

Rafik Affes, Jean-Yves Delenne, Yann Monerie, Farhang Radjai, Vincent Topin. Tensile strength and fracture of cemented granular aggregates. European Physical Journal E: Soft matter and biological physics, 2012, 35 (11), 10.1140/epje/i2012-12117-7 . hal-01268264

HAL Id: hal-01268264
https://hal.science/hal-01268264

Submitted on 9 Apr 2019

HAL is a multi-disciplinary open access archive for the deposit and dissemination of scientific research documents, whether they are published or not. The documents may come from teaching and research institutions in France or abroad, or from public or private research centers.

L'archive ouverte pluridisciplinaire **HAL**, est destinée au dépôt et à la diffusion de documents scientifiques de niveau recherche, publiés ou non, émanant des établissements d'enseignement et de recherche français ou étrangers, des laboratoires publics ou privés.

Eur. Phys. J. E (2012) **35**: 117
DOI 10.1140/epje/i2012-12117-7

THE EUROPEAN PHYSICAL JOURNAL E

Regular Article

Tensile strength and fracture of cemented granular aggregates

R. Affes[1,3,a], J.-Y. Delenne[3,4], Y. Monerie[2,3], F. Radjaï[1,3], and V. Topin[2,3]

[1] Université Montpellier 2, CNRS, LMGC, Place Eugène Bataillon, F-34095 Montpellier cedex, France
[2] IRSN, PSN, CE Cadarache, Bat. 702, BP3-13115 St. Paul-lez-Durance Cedex, France
[3] Laboratoire MIST, IRSN-CNRS-Université Montpellier 2, France
[4] IATE, UMR1208 INRA-CIRAD-Montpellier Supagro-UM2, 2 place Pierre Viala - 34060 Montpellier cedex 01, France

Received 24 June 2012 and Received in final form 25 September 2012
Published online: 20 November 2012 – © EDP Sciences / Società Italiana di Fisica / Springer-Verlag 2012

Abstract. Cemented granular aggregates include a broad class of geomaterials such as sedimentary rocks and some biomaterials such as the wheat endosperm. We present a 3D lattice element method for the simulation of such materials, modeled as a jammed assembly of particles bound together by a matrix partially filling the interstitial space. From extensive simulation data, we analyze the mechanical properties of aggregates subjected to tensile loading as a function of matrix volume fraction and particle-matrix adhesion. We observe a linear elastic behavior followed by a brutal failure along a fracture surface. The effective stiffness before failure increases almost linearly with the matrix volume fraction. We show that the tensile strength of the aggregates increases with both the increasing tensile strength at the particle-matrix interface and decreasing stress concentration as a function of matrix volume fraction. The proportion of broken bonds in the particle phase reveals a range of values of the particle-matrix adhesion and matrix volume fraction for which the cracks bypass the particles and hence no particle damage occurs. This limit is shown to depend on the relative toughness of the particle-matrix interface with respect to the particles.

1 Introduction

Cemented aggregates of solid particles are very common in nature and an essential ingredient of many industrial products. Well-known examples are sedimentary rocks such as sandstones and conglomerates [1], mortars, concrete, bituminous concrete [2–4], grouted soils [5], and biomaterials such as the wheat endosperm composed of starch granules bound together by a protein matrix [6, 7]. The common denominator of all these materials is to be composed of a dense granular assembly cemented by a paste partially filling the pore space. They may be described as intermediate materials between particle-reinforced composites and cohesionless granular media. The cementing paste endows the aggregate with macroscopic cohesion but, in contrast to particle-reinforced composites, the mechanical properties are strongly controlled by the granular backbone [8]. Hence, cemented aggregates are more complex than cohesive granular materials with surface adhesion between grains such as fine powders [9–12] due to the bulk effect of the matrix, which makes the mechanical behavior depend not only on the granular backbone but also on load transfer between the grains and the matrix [13–15]. For this reason, a multitude of physical mechanisms (interface debonding, particle fracture, matrix deformation, etc.) control the deformation and failure of cemented aggregates that are generally difficult to isolate from experiments or to predict theoretically [16–18].

Another important feature of cemented aggregates is that the pore space is often only partially filled by the matrix. In particular, they generally involve microcleavages or bare contacts (no interposed matrix) between the grains [13,19]. For example, there is experimental evidence that the contact zones in grouted sand are not all cemented and the cohesion is ensured only by the grain-matrix adhesion [5]. The bare contacts behave as microcracks and lead to reduced stiffness and strength in both tension and compression. For this reason, the formulation of concrete requires an overfilling cement, *i.e.* the cement exceeding the minimum content that would fill the voids of the fully packed grains [19]. The porosity is also monitored by means of the particle size distribution, which allows for largest pores to be filled by finer particles. The adhesion of the cement to the grains and the defects in the contact zone between the grains are as important as its volume for load-bearing capacity of concrete [4,17,20].

The theoretical and numerical models developed for cohesionless granular aggregates or particle-reinforced composites are often inappropriate for cemented granular aggregates. Discrete element modeling (DEM) is a powerful approach for the simulation of granular materials composed of rigid particles [21–26]. However, cohesive

[a] e-mail: rafik.affes@univ-montp2.fr

behavior in DEM simulations may be introduced only in terms of force laws at the contact point [27–30] or by connecting the particles by rigid beams [31–35]. In such models, the bulk effect of a cementing matrix cannot be taken into account. On the other hand, particle-reinforced composites may be modeled by means of analytical methods [36–39] or numerical approaches [40,41] based on continuum mechanics and used essentially to compute the elastic properties of composite systems. In cemented aggregates the microstructure is highly complex because of both its multiphase nature and the intrinsic disorder of its granular structure, which involves an inhomogeneous stress transmission. Hence, the application of analytical and finite element methods (FEM) is almost unfeasible for a representative volume element of the material with a large number of embedded particles.

In order to be able to simulate complex microstructures, a trade-off is necessary between numerical efficiency and physical description of the system. Such a compromise is provided by the lattice element method (LEM), which has been recently applied for the simulation of 2D cemented aggregates [8]. In this method, the space is discretized on a regular or irregular lattice of 1D elements, which can be simple harmonic springs or beams with an elastic brittle behavior [42–44]. These lattice elements belong to different bulk or interface phases (particle, matrix, void, particle-matrix interface, particle-particle interface) with different properties (stiffness, failure threshold) representing the nature of each phase. This approach accounts for breakable interface elements (as interparticle contacts in a granular media) and breakable bulk elements (as a damageable volume element in continua). Using simple elastic-brittle bonds allows for the simulation of large systems involving a large number of particles with variable volume fraction of the binding phase. Lattice-type discretization has been extensively used for the statistical mechanics of fracture in disordered media, and applied to study the fracture properties of concrete and ceramics [43,45–54].

In this paper, we employ LEM simulations for a detailed analysis of 3D cemented aggregates composed of a dense packing of spherical particles with variable matrix volume fraction and particle-matrix adhesion under tensile loading. We investigate the effective stiffness, tensile strength, stress transmission and failure of cemented aggregates by focusing on the respective roles of matrix volume fraction and particle-matrix adhesion. For the effective stiffness, we also evaluate the influence of finite spatial resolution and compare the data with the prediction of analytical models developed for composites. The influence of granular structure is studied by considering the distribution of node stresses. A fundamental issue in this respect is whether the broad inhomogeneous force distributions observed in cohesionless granular media (under compressive forces) are relevant under tensile loading, and how the distributions are affected by load transfer from the particle phase to the matrix phase as the matrix volume fraction is increased.

We are also interested in the tensile strength and mechanisms of failure by the generation and propagation of cracks as a result of the rupture of lattice elements. In particular, we show that, depending on whether the binding phase percolates throughout the system and the strength of adhesion at the particle-matrix interface, the cracks may propagate either in the matrix phase or across the particles producing a superficial or core damage. We discuss whether a single material parameter combining matrix volume fraction and particle-matrix adhesion may be defined to scale the strength and particle damage data. Our 3D simulations and results provide the opportunity for comparison with both experiments performed with model granular aggregates [55] and 2D LEM simulations of disk packings [8].

In the following, we first introduce in sect. 2 the physical model and numerical procedures used for the simulations. Then, in sect. 3, we focus on the stress-strain behavior and elastic stiffness. The stress transmission is analyzed in sect. 4. Section 5 is devoted to the tensile strength and its scaling with matrix volume fraction. In sect. 6, we analyze crack paths and particle damage. Finally, in sect. 7, we conclude with the most salient results and perspectives of this work. Most technical aspects are presented in separate appendices.

2 Numerical procedures

2.1 Lattice element method

The lattice element method (LEM) is based on the discretization of different phases of a solid on a regular or irregular lattice [8,56,57]. Hence, the space is represented by a grid of points (nodes) interconnected by one-dimensional elements (bonds). Each bond can transfer normal force, shear force and bending moment up to a threshold in force or energy, representing the cohesion of the phase or its interface with another phase. In its simplest version, the elements are linear springs characterized by a Hooke constant and a breaking threshold.

Each bulk phase (particle, matrix, pores) or surface phase (interface between two bulk phases) is materialized by the bonds carrying the properties of that phase. The samples are deformed by imposing displacements or forces to nodes belonging to the contour. The total elastic energy of the system is a convex function of node displacements so that finding the unique equilibrium configuration of the nodes amounts to a minimization problem. Performing this minimization for stepwise loading corresponds to subjecting the system to a quasistatic deformation process. Alternatively, the system of equations can be integrated by explicit time-stepping schemes as in molecular dynamics. We developed a 3D LEM algorithm based on a conjugate-gradient solver. A brief description of the method is given in appendix A.

LEM has the advantage of allowing for the initiation and propagation of cracks by simply breaking the critical elements, *i.e.* the elements carrying a force above a breaking threshold. The effective behavior is elastic brittle with elastic moduli depending on the lattice geometry and single-element characteristics. A fully irregular lattice

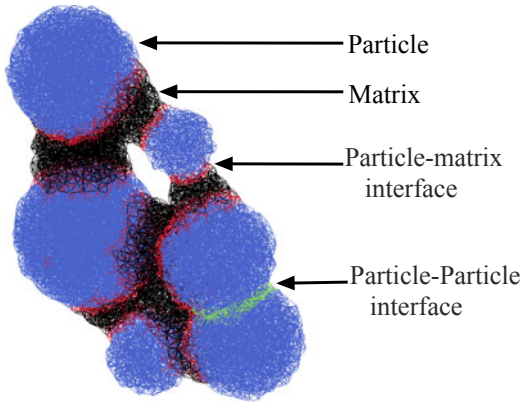

Fig. 1. Lattice representation of a granular aggregate composed of particles, solid matrix connecting the particles and voids.

with random orientations of all elements represented by simple springs of the same Hooke constant k corresponds to an isotropic medium of Young's modulus $E = 3\sqrt{2}k/5$ and Poisson ratio $\nu = 1/4$; see appendix B. The macroscopic breaking threshold depends on the lattice disorder and local thresholds. In porous granular aggregates considered in this paper, the main source of disorder is the random spatial distribution of the particles and the matrix phase.

2.2 System description

We first generate a large dense packing of rigid spheres compacted isotropically by means of a discrete element method in a cubic box. A cubic portion of this packing is overlaid on a random 3D tetrahedral lattice. The binding matrix is then introduced in the form of truncated conical bridges of variable thickness connecting neighboring particles within a prescribed distance; see fig. 1. The total volume of the binding matrix is distributed among the eligible pairs of particles proportionally to the mean square diameter of each pair. Hence, at low matrix volume fraction, the matrix occurs basically in the form of conical bridges joining neighboring particles. As the matrix volume fraction is increased, the bridges begin to overlap and percolate at some point throughout the packing. The bonds belonging to these bridges are given the properties of the binding matrix whereas those within the particles have the properties of the particle phase. In the same way, the bonds located between a particle and the matrix or between two particles are given the desired properties of the corresponding interface.

In the simulations reported in this paper, the underlying lattice bonds are simple springs characterized by a Hooke constant and a breaking force threshold. A lattice of beam-like elements leads to a more realistic behavior of crack propagation for shear and distortion when the characteristics of the beams are uniform throughout the system with some degree of bond disorder. In our system, the material behavior reflects to a lesser extent the lattice characteristics than structural disorder at the scale of the particles, each particle being represented by a collection of hundreds of elements. For example, the tortuosity of the cracks is mainly controlled by the contrast between the bonds belonging to the matrix and those belonging to the particles as well as by the particle size distribution. The cracks propagate along straight lines and may be deflected by the particles. It is also important to note that we consider only small strains so that the topology of lattice is not alterned during deformation. Hence, the strength of the lattice in shear and distortion is ensured by the high connectivity of the nodes. For these reasons, the spring-like elements lead to a rather realistic behavior in our simulations. Another important parameter is computation time, which is reduced by a factor of the order of 3 when using springs instead of beam-like bonds.

The samples consist of the bulk phases: 1) particles, denoted "p"; 2) matrix, denoted "m"; and 3) void space or pores, denoted "v", as well as the interface phases: 1) particle-particle interface, denoted "pp", and 2) particle-matrix interface, denoted "pm". The elements belonging to each phase ϕ (bulk or interface) are given a Hooke constant k^ϕ and a breaking force f^ϕ. We have $f^v = 0$ and the choice of the value of k^v is immaterial.

The surface phases "pm" and "pp" are mono-element transition zones linking two particles or a particle to the matrix. The interface phases affect the global behavior through their specific surfaces (total surface per unit volume) and their strengths represented by the Hooke constants k^{pp} and k^{pm}, and the corresponding tensile force thresholds f^{pp} and f^{pm}. It is noteworthy that, depending on the fineness of discretization, the volume of the interface zones in a discrete representation may not be negligible compared to that of the bulk phases. The volume of the interface may be partially or fully attributed to either of the two bulk phases depending on the mechanical problem at hand. For example, in dealing with the effective stiffness as a function of the matrix volume fraction, the latter needs to be adjusted by requiring that the tensile stiffness vanishes at $\rho^m = 0$; see sect. 3.

It is dimensionally convenient to express the bond characteristics in stress units. We thus define the bond breaking (or debonding) stresses $\sigma^\phi \equiv f^\phi/a^2$ and the moduli $E^\phi \equiv k^\phi/a$, where a is the average length of the elements. These bond moduli E^ϕ of the lattice are obviously distinct from the effective phase moduli which depend on both the bond moduli and geometry of the lattice. We will use below square brackets to represent the effective phase moduli: $E^{[p]}$, $E^{[m]}$, $E^{[pp]}$ and $E^{[pm]}$. In a granular aggregate, the effective tensile strength σ_{eff} of the system and the effective Young's modulus E_{eff} depend on the breaking characteristics σ^ϕ and phase moduli E^ϕ, the geometry of the lattice and the spatial distributions of the phases. The main elastic parameters that will be considered in this paper are the Hooke constants k^p and k^m of the bonds belonging to the particles and matrix, respectively. The initial state is the reference (unstressed) configuration. When the sample is loaded, bond forces develop inside the sample.

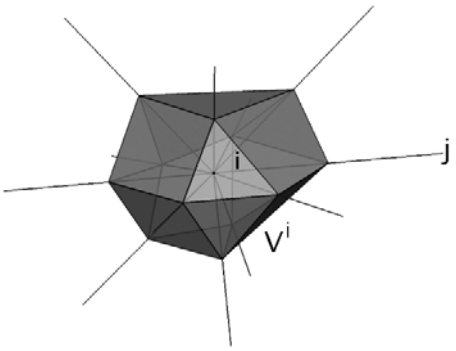

Fig. 2. A node i with its neighbors j and the corresponding Voronoi cell for the definition of node stress.

A stress tensor $\boldsymbol{\sigma}^i$ can be attributed to each node i of the lattice network

$$\sigma^i_{\alpha\beta} = \frac{1}{|V^i|} \sum_j r^{ij}_\alpha f^{ij}_\beta, \tag{1}$$

where the summation runs over all neighboring nodes j, r^{ij}_α is the α component of the vector joining the node i to the midpoint of the bond ij and f^{ij}_β is the β component of the bond force [57,58]; see appendix C for more details. In the stress maps of granular agglomerates each component σ^α_{ij} is represented by a proportional color intensity or grey level over the elementary Voronoi cell centered on the node i (volume $|V^i|$); see fig. 2.

2.3 Simulation parameters

In LEM calculations of cemented aggregates, the precision depends on the number of lattice elements per particle. On the other hand, for a good statistical representativity of a sample, a minimum number of particles are required. In the parametric studies reported in this paper, the samples are of cubic shape, containing each 516 particles of diameters uniformly distributed between $d_{\min}$ and $d_{\max} = 1.25 d_{\min}$. The particle volume fraction is $\rho^p \simeq 0.64$. The samples are meshed by $M \simeq 1.3 \times 10^6$ elements and each particle contains about 1550 elements. These parameter values provide a good compromise between the numerical efficiency, precision and representativity of the structure. Given the spatial resolution, the particle shapes may be considered as spheres with a rough surface. The roughness is of the order of $2a/d \simeq 0.2$, where d is the average particle diameter.

Eight samples were prepared with the following values of the matrix volume fraction ρ^m: 0.06, 0.1, 0.13, 0.17, 0.2, 0.22, 0.24 and 0.28. The matrix is distributed equally to all pairs of particles separated by a distance $\delta \leq d_{\min}$. In all samples, except in fig. 5, we set $\sigma^{pp} = 0$, which corresponds to "bare" contacts between particles with vanishing tensile strength. This choice is motivated by the observation that in most cemented aggregates such as conglomerates and concrete the binding material is the only source of adhesion. The direct contact points between particles

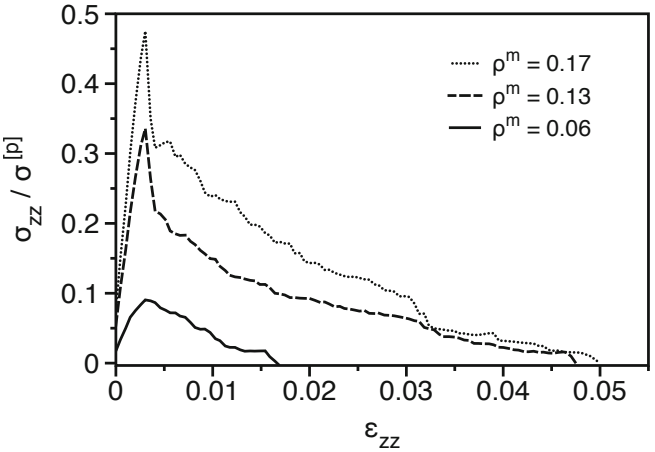

Fig. 3. Vertical tensile stress normalized by the tensile strength $\sigma^{[p]}$ of the particles as a function of vertical strain for different values of the matrix volume fraction ρ^m.

are therefore the weak points of the material, which can be considered as micro-cracks or cleavages where the cracks are initiated. Obviously, such contacts are eligible for receiving the matrix only outside the contact zone. Note also that, because of the thickness of the particle-particle interface due to finite spatial resolution, the pores between particles are filled by the matrix for $\rho^m = 0.28$ (this would have been 0.34 if the thickness were zero).

The particles are assumed to be three times stiffer than the matrix ($E^p = 3E^{pm} = 3E^m$) as usually observed in concrete. We also set $\sigma^p = \sigma^m$ in order to avoid in the parametric studies the effects related to the proper strength of the particles. Although such effects need to be investigated later, we focus in this paper on the particle-matrix adhesion and matrix volume fraction. As to the particle-matrix adhesion σ^{pm}, its value for each configuration was varied from $0.2\sigma^p$ to $1.4\sigma^p$. In this way, a total number of 81 simulations were performed for the parametric studies analyzed in this paper.

Assuming that the chosen computational cells reach the size of the Representative Volume Element, affine displacement boundary conditions are applied. For tensile loading, the vertical positions of the bottom nodes of each sample are fixed and upward displacement increments of $3 \times 10^{-4} a$ are applied to the top nodes. All other surface nodes of the samples are free with a null confining stress. The simulation ends when the tensile stress vanishes. The CPU time is on the average 0.025 s per displacement increment and per node before failure on a 2.93 GHz Intel Xeon processor. Video samples of some of the simulations analyzed below can be found at `www.cgp-gateway.org/ref017`.

3 Elastic behavior

Typical examples of strain-stress behavior are displayed in fig. 3 where the vertical stress σ_{zz} is plotted as a function of the cumulative vertical strain ε_{zz} for three different

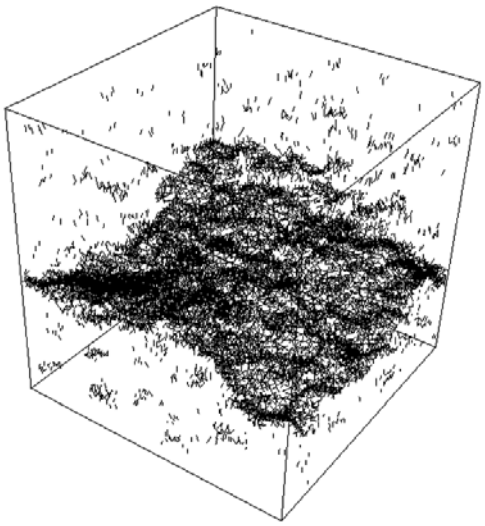

Fig. 4. 3D map of broken bonds (black segments) in the post-failure regime.

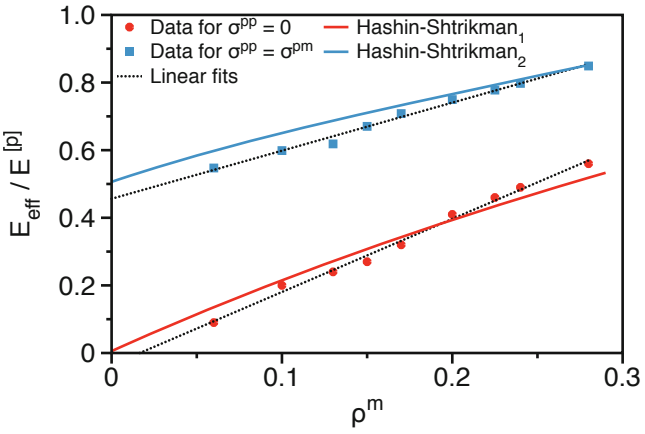

Fig. 5. Normalized effective initial Youngs moduli with bare contacts between particles ($\sigma^{pp} = 0$, red) and with adhesive contacts ($\sigma^{pp} = \sigma^{pm}$, blue) together with linear fits (dotted lines): numerical results (symbols), Hashin-Shtrikman-type estimates (lines, see appendix D).

values of ρ^m and for $\sigma^{pm} = 0.3\sigma^p$. The stresses are normalized by the tensile strength $\sigma^{[p]} = \sigma^{[m]}$ of the particles and matrix. We observe an initial linear elastic behavior with a well-defined stiffness E_{eff} followed by a nonlinear regime up to failure at $\sigma_{zz} = \sigma_{\text{eff}}$. Since the lateral confining stress is zero in our simulations, E_{eff} represents the effective Young modulus of the material. The post-failure regime is characterized by an abrupt fall-off followed by a gradual decrease of tensile stress until the full disruption of the sample. The peak stress increases with ρ^m and is reached for a deformation $\varepsilon_{zz} \simeq 4 \times 10^{-3}$.

The nonlinear rising regime corresponds to progressive degradation of the material due to diffuse breaking of the bonds. The sample yields when a fracture surface emerges from diffuse cracks and propagates across the sample. Generally, a single fracture surface survives and propagates, causing the separation of the sample into two blocks. One example of the broken bonds and rupture surface is shown in fig. 4. The post-failure damage in our 3D simulations appears to be much more progressive than in 2D simulations [8]. In fact, a 2D sample breaks apart simply by a line of broken bonds across the sample whereas a 3D sample will keep its mechanical integrity unless a fracture surface is formed.

The evolution of the effective Young's modulus E_{eff} with ρ^m is displayed in fig. 5 for our system with bare contacts between particles ($\sigma^{pp} = 0$) and for the same samples with the same tensile strength between particles as that of particles with the matrix ($\sigma^{pp} = \sigma^{pm}$). For all simulated samples and in both cases, E_{eff} is a clear-cut linear function of ρ^m. The observed values of the effective Young's modulus are below the Young's modulus of the particle phase since tensile loading affects mainly the matrix phase, which is three times less stiff than the particles. But we also see that, due to the presence of the particles, for high matrix volume fractions Young's modulus rises to values of the order of 1.6 and 2.5 times Young's modulus of the matrix phase with bare and adhesive contacts between particles, respectively. With adhesive contacts between particles, the effective Young's modulus approaches that of the particles since tensile stresses can also be directly sustained by the contact network. This is also true under compressive loading, since the contraction of the packing affects the contact zones between particles as observed previously in 2D cemented aggregates [8,59].

It is interesting to compare the effective stiffness calculated from the simulation data with the predictions of analytical field theories of elastic strains in an infinite homogeneous medium containing inclusions of simple shape [60]. Our numerical results are in agreement with the predictions of analytical Hashin-Shtrikman-type estimates detailed in appendix D, when considering a three-phase composite made of a matrix interphase, a collection of spherical pores and a collection of spherical particles randomly distributed in space.

In analyzing the effective Young's modulus as a function of matrix volume fraction, the numerical parameters such as the total number of bonds M and the configuration of the particles were kept the same in all simulations. But, since the volume is discretized independently of the microstructure, a property may be correctly attributed to a bond only if it belongs entirely to a phase. Irrespective of discretization, random or structured, there is thus always a misfit between the meshed microstructure and the true microstructure. In the case of FEM simulations, this finite spatial resolution is known to affect the effective elastic properties and an insufficient number of elements or meshes in a solid region may not represent correctly continuum elasticity [61,62]. In order to evaluate such discretization errors in the LEM simulations, we studied Young's modulus E_{eff} at increasing number of elements M in two limit cases: a solid matrix containing a random distribution of 20% of i) stiff spherical inclusions, ten times stiffer than the matrix and ii) spherical pores. Figure 6 shows the corresponding effective Young's modulus E_{eff} as a function of the average mesh density $L_n = 1/M^{1/3}$ in

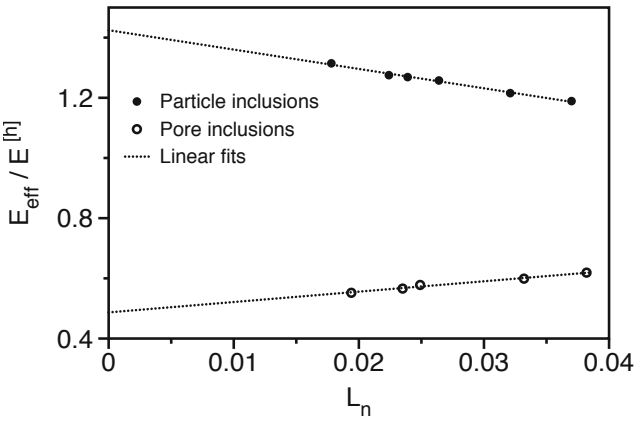

Fig. 6. Normalized effective Young's modulus for a material with hard inclusions or with porous inclusions as a function of the mesh density (symbols) and linear fits (dotted lines).

both cases. As in FEM simulations, we observe a linear dependence with an increasing stiffness in the first case and a decreasing stiffness in the second case as the resolution increases (decreasing L_n):

$$\frac{E_{\text{eff}}}{E^{[p]}} \simeq \left.\frac{E_{\text{eff}}}{E^{[p]}}\right|_0 + \alpha_E L_n,$$

where α_E is a dimensionless coefficient and $E_{\text{eff}}/E^{[p]}|_0$ represents the "exact" value of normalized Young's modulus $E_{\text{eff}}/E^{[p]}$ for a vanishing mesh size (mesh density L_n tends to zero and global number of bounds M tends to $+\infty$). The linear fit to data points makes it possible to evaluate this exact value. In the following, all situations analyzed in this paper are carried out with $L_n \simeq 0.01$ so that the possible relative errors in the apparent elastic properties, compared to the exact value, are below 10%.

4 Stress transmission

Stress transmission in granular materials is featured by highly loaded contact chains sustaining nearly the whole shear stress [59, 63]. In a dense cemented aggregate, the stress chains may still occur due to higher stiffness of the particles and their high connectivity. From the simulations, we have access to the node stresses in the matrix, particles and their interface; see appendix C. Maps of uniaxial node stresses σ^i_{zz} are displayed in fig. 7 for three values of the matrix volume fraction. We observe both tensile and compressive vertical stresses while the aggregate is subjected to vertical tensile loading. Chains of strong tensile stresses cross the particles and a higher stress concentration is observed at the contact zones between particles as in granular materials.

The probability density function (pdf) of the vertical components of node stresses σ^i_{zz} is shown in fig. 8 for the same values of the matrix volume fraction. The strong tensile stresses fall off exponentially

$$P(\sigma^i_{zz}) \propto e^{-\beta\sigma^i_{zz}/\sigma_{zz}}. \qquad (2)$$

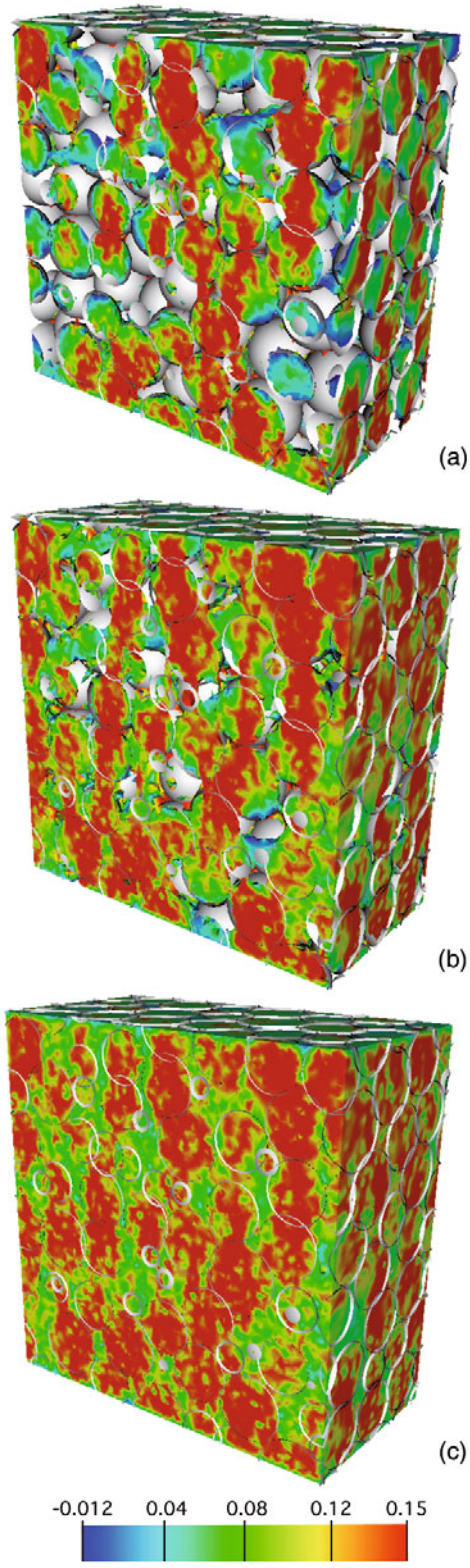

Fig. 7. A color map of vertical stresses σ_{zz} at the center of a cemented aggregate under tensile loading for three different values of the matrix volume fraction: (a) 0.06, (b) 0.17 and (c) 0.28. The color scale shows the range of tensile (positive) and compressive (negative) stresses.

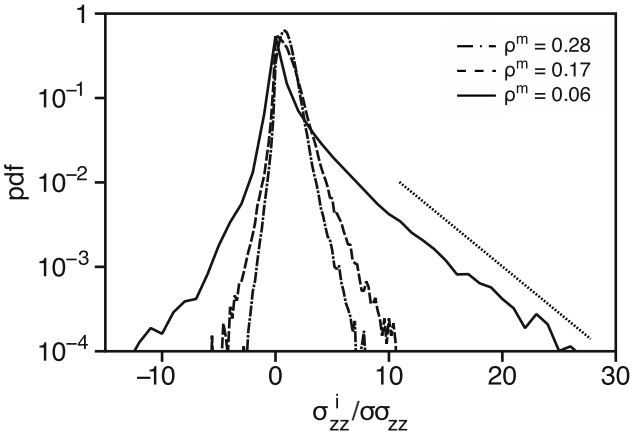

Fig. 8. Probability density function (pdf) of vertical node stresses σ^i_{zz} normalized by the applied tensile load for three levels of matrix volume fraction; see fig. 7. The dotted line indicates the exponential tail of the pdf in the range of strong tensile stresses.

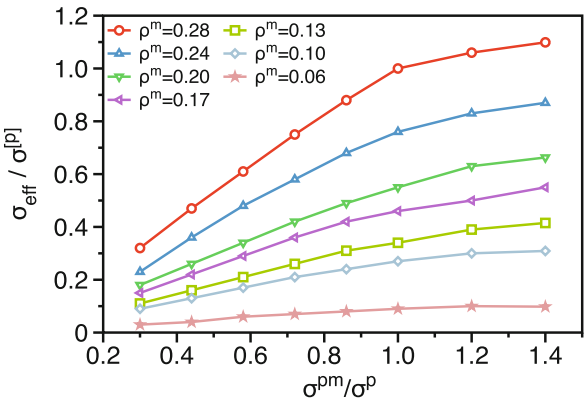

Fig. 9. Tensile strength as a function of particle-matrix adhesion for different values of matrix volume fraction.

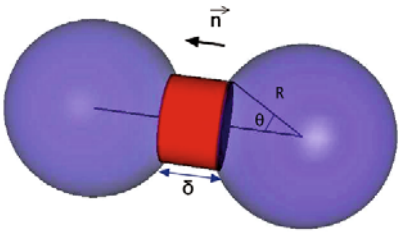

Fig. 10. A pair of particles joined by a cylindrical bridge of length δ and filling angle θ.

The exponential distribution is a hallmark of strong contact forces in cohesionless and cohesive granular media [64–67]. The weak tensile (positive) and compressive (negative) stresses have a nonzero pdf in analogy to weak contact forces in granular materials and reflect the arching effect [63, 65, 68].

Despite the smaller range of compressive stresses, they seem to follow an exponential fall-off as strong tensile stresses. As compared to stress distribution previously obtained for 2D aggregates [8, 59], the 3D distributions are broader and reveal a higher degree of inhomogeneity. The pdf is increasingly broader for decreasing matrix content as the stresses become more concentrated in the matrix bridges between the particles. The exponent β varies from $\simeq 0.7$ to $\simeq 2.1$ as ρ^m increases from 0.06 to 0.28. We find similar behavior for other components of the stress tensor.

This striking similarity of stress distributions to force distributions in granular media, up to variations in the range of forces as a function of matrix volume fraction, indicates that stress concentration in cemented aggregates is mainly controlled by contact network disorder. This is a distinctive feature of cemented granular aggregates compared to composites where stress concentration is mainly dependent on the pore space, *e.g.* [69].

5 Tensile strength

The failure of aggregates is initiated by diffuse debonding in the whole volume of the composite and accelerated by the coalescence of micro-cracks along a rupture surface. Since the matrix and particle phase have the same tensile strength ($\sigma^{[p]} = \sigma^{[m]}$) and the particle-particle contacts have no adhesion ($\sigma^{pp} = 0$), the effective tensile strength of the material depends on the particle-matrix adhesion σ^{pm} and the matrix volume fraction ρ^m, which controls the porosity of the aggregate.

The effective tensile strength σ_{eff}, defined as the peak stress in the effective stress-strain response, is an increasing function of both the matrix volume fraction ρ^m and particle-matrix adhesion σ^{pm} as shown in fig. 9. The particle-matrix interface is reinforced by increasing σ^{pm} with the effect of hindering the propagation of cracks. This effect is less pronounced at low values of ρ^m (high porosity) where stress transmission is governed by the pore space rather than particle-matrix interface. At higher values of ρ^m the role of the interface zones prevails and the tensile strength grows rapidly with σ^{pm}.

It is remarkable that in the range $\sigma^{pm} > \sigma^{[p]}$, the tensile strength continues to increase with σ^{pm} though with a trend to saturate. The particle-matrix interface with an adhesion above the internal adhesion of each phase behaves as a hard coating, which protects the particles from cracking or from the penetration of cracks initiated in the matrix. Due to this "coating effect", the largest value of σ_{eff} is slightly above $\sigma^{[p]}$ for $\sigma^{pm} > \sigma^{[p]}$ in the absence of pores ($\rho^m = 0.28$).

In order to understand the effect of ρ^m, we distinguish between 1) the matrix bridges between particles, which are responsible for stress transmission in the particle phase under tensile loading (binding effect), and 2) bulk transmission of tensile stresses in the matrix phase (bulk effect). Let us consider two particles of the same radius R joined by a cylindrical matrix bridge, as displayed in fig. 10. The total area of the two particles covered by the matrix is given by

$$S = 4\pi R^2(1 - \cos\theta), \tag{3}$$

where θ is the filling angle.

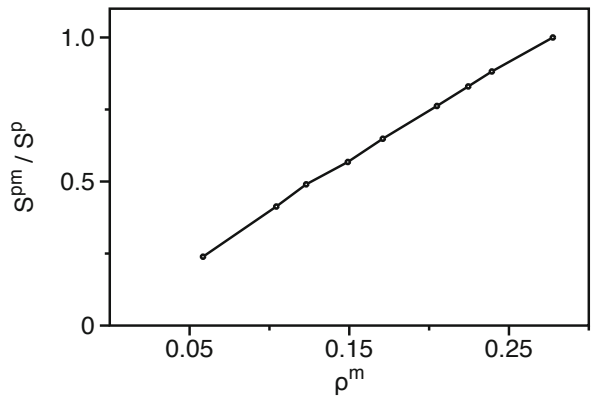

Fig. 11. Particle-matrix interface area normalized by the total surface of the particles as a function of matrix volume fraction.

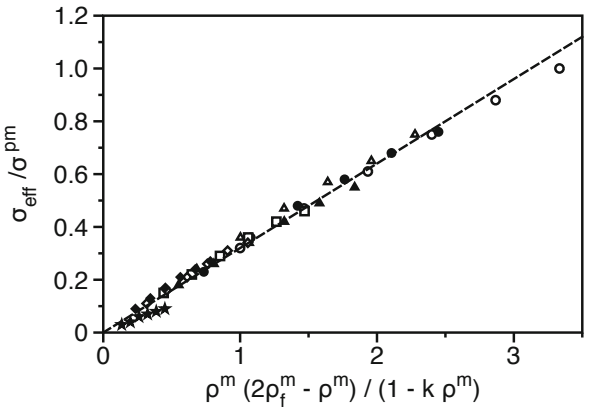

Fig. 12. The scaling of tensile strength normalized by the particle-matrix adhesion with the matrix volume fraction. The dashed line indicates the mean trend according to eq. (10) for $k = 2.5$. The symbol labels, corresponding to those of fig. 9, are omitted.

The largest tensile force supported by a particle-matrix interface element $\boldsymbol{n}'\mathrm{d}S$, where $\boldsymbol{n}'$ is the outward normal to the particle surface, is $\mathrm{d}\boldsymbol{f} = \sigma^{pm}\boldsymbol{n}'\mathrm{d}S$. Hence, the largest tensile force f_c sustained by the bridge is obtained by integrating the projection of $\mathrm{d}\boldsymbol{f}$ along the bridge axis $\boldsymbol{n}$ over the covered area

$$f_c = \int_{\text{covered area}} \boldsymbol{n}\cdot\mathrm{d}\boldsymbol{f} = \frac{1}{2}\pi R^2\sigma^{pm}(1-\cos 2\theta). \quad (4)$$

This force may be expressed as a function of the local specific surface $S' = S/(4\pi R^2)$ by eliminating θ between (3) and (4)

$$f_c = \pi R^2\sigma^{pm}S'(2-S'). \quad (5)$$

The factor $2 - S'$ reflects the curvature of the interface. This equation shows that f_c is an increasing function of S' and reaches its highest value $\pi R^2\sigma^{pm}$ for $S' = 1$.

In a mean-field approach, we neglect the small-size polydispersity of the particles and f_c may be replaced by the average tensile force between particles at failure. In the same way, S' represents the particle-matrix interface specific area S^{pm}, defined as the covered area normalized by the total area S^p of the particles. Figure 11 shows S^{pm} as a function of the matrix volume fraction ρ^m. The specific area S^{pm} increases linearly with ρ^m, and the particles are fully covered by the matrix ($S^{pm} = 1$) only when the pore space is filled ($\rho^m = \rho_f^m = 0.28$). This is a consequence of the filling procedure by increasing the diameter of matrix bridges among particles. We thus get a simple relation,

$$\frac{S^{pm}}{S^p} = \frac{\rho^m}{0.28} = \frac{\rho^m}{\rho_f^m}, \quad (6)$$

which, with the assumption that the average behavior is a consequence of the local force model of eq. (5), leads to the following expression for the mean tensile force:

$$\langle f_c\rangle = \pi R^2\sigma^{pm}\frac{\rho^m}{\rho_f^m}\left(2-\frac{\rho^m}{\rho_f^m}\right). \quad (7)$$

Again, in a mean-field approximation, the average tensile stress σ_{eff}^p sustained by the matrix bridges between particles is proportional to the mean force $\langle f_c\rangle$ divided by the average particle cross section πR^2

$$\sigma_{\text{eff}}^p \propto \sigma^{pm}\frac{\rho^m}{\rho_f^m}\left(2-\frac{\rho^m}{\rho_f^m}\right). \quad (8)$$

The proportionality factor is a function only of the packing structure and number of matrix bridges per particle. The latter is of the order of 9 and does not evolve with ρ^m in exception to the lowest value $\rho^m = 0.06$ for which not all contacting particles are connected by a matrix bridge and the number of matrix bridges per particles is about 6.

The tensile stress σ_{eff}^p represents a fraction of the total stress σ_{eff} at failure. With increasing ρ^m, an increasing fraction of the tensile load is transferred to the bulk of the matrix phase. Assuming that this fraction is a linear function of ρ^m, we have

$$\sigma_{\text{eff}}^p = (1-k\rho^m)\sigma_{\text{eff}}, \quad (9)$$

where k is a constant independent of ρ^m. This relation, together with eq. (8), leads finally to the following scaling of tensile strength:

$$\frac{\sigma_{\text{eff}}}{\sigma^{pm}} = A\frac{\rho^m(2\rho_f^m-\rho^m)}{1-k\rho^m}, \quad (10)$$

where A is a packing constant.

In fig. 12, all our normalized tensile strength data $\sigma_{\text{eff}}/\sigma^{pm}$ from fig. 9 are plotted as a function of $\rho^m(2\rho_f^m - \rho^m)/(1-k\rho^m)$. We see that nearly all data points collapse on a straight line by setting $k \simeq 2.5$ and $A \simeq 0.3$. The data corresponding to $\rho^m = 0.06$ show a slightly lower slope ($\simeq 0.2$) which is consistent with the lower connectivity of the particles in this limit.

6 Crack regimes and particle damage

In lattice models of fracture, the number of broken elements is often used as a measure of damage [49]. In a

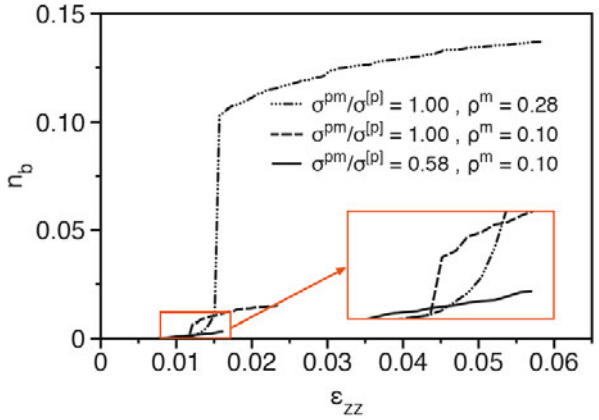

Fig. 13. Proportion of broken bonds inside the particle phase as a function of vertical strain for different values of parameters. The inset is a zoom.

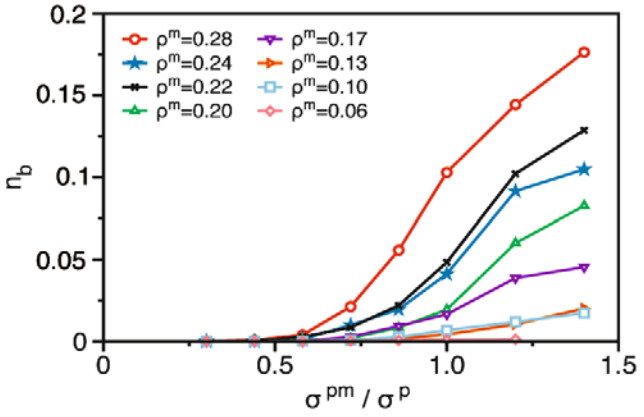

Fig. 14. Proportion of broken bonds inside the particles after failure as a function of particle-matrix adhesion for different values of matrix volume fraction.

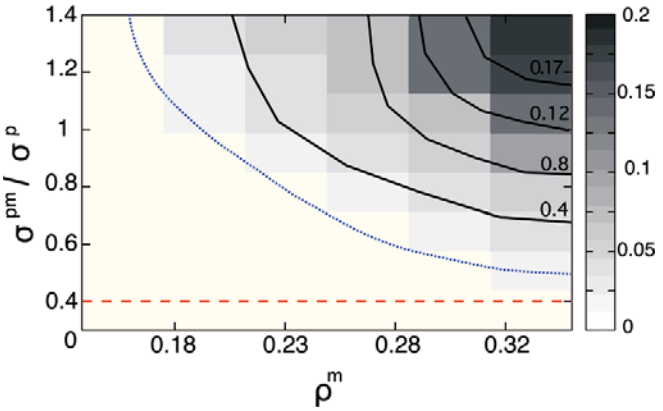

Fig. 15. Grey-level map of the proportion of broken bonds in the particle phase for various values of the matrix volume fraction ρ^m and particle-matrix interface strength σ^{pm}. The dashed line represents the weakest link approach (eq. (13) with $K_c^r = 0.4$). The dotted curve represents the "particle damage limit" (eq. (14) with $K_c^r = 0.7$).

cemented aggregate, the broken bonds may happen in the matrix, in the particle phase or at their interface. We consider here the proportion n_b of broken bonds inside the particles compared to the total number of broken bonds in the whole aggregate. The limit case $n_b = 0$ corresponds to a situation where the particles are not damaged and the micro and macro cracks propagate only in the matrix phase or along the particle-matrix interface. The limit $n_b = 1$ corresponds to an aggregate where the particles are much more brittle than the matrix and break down under tensile loading. In our system with the choice $\sigma^p = \sigma^m$, the cracks propagate from the bare contacts between particles or from the initially broken bonds at the most loaded elements at the interface, and they may penetrate more or less easily into the particles depending on the properties of the particle-matrix interface. Hence, the evolution of n_b provides an interesting indicator of particle damage and crack paths.

Figure 13 shows the evolution of n_b as a function of axial strain for three different sets of parameters. For low enough values of σ^{pm}, particle damage is negligibly small irrespective of the matrix volume fraction ρ^m. Obviously, the cracks propagate in this case favorably along the particle-matrix interface. At high levels of σ^{pm}, n_b remains small up to the yield point at which it rapidly increases as a result of rupture along a fracture surface, and then continues to increase slowly during the post-failure phase.

Figure 14 displays n_b just after failure as a function of σ^{pm} for different values of ρ^m. We see that n_b begins to increase from zero only for a finite value of σ^{pm} that depends on ρ^m. Thereafter, the increase of n_b with σ^{pm} is nonlinear: increasing rate followed by a decreasing rate with an inflection point at $\sigma^{pm} \simeq \sigma^p$. The number of broken bonds in the particle phase is also an increasing function of matrix volume fraction ρ^m. Note that for the lowest value $\rho^m = 0.06$, the number of broken bonds n_b remains vanishingly small.

A grey-level map of n_b in the parameter space (ρ^m, σ^{pm}) is shown in fig. 15. Below a well-defined frontier (marked by a dotted line), no particle damage occurs ($n_b \simeq 0$). This means that, for this range of parameter values, corresponding essentially to low values of ρ^m or σ^{pm}, the cracks propagate either in the matrix or at the particle-matrix interface. Above this "particle damage" limit, the iso-level lines of n_b are similar to the limit line with increasing n_b. The map is comparable to that of 2D cemented aggregates investigated in [8] with a major difference that in 3D no change of behavior is observed for a critical value of ρ^m. We simply distinguish here two regimes: 1) below the particle-damage limit, the cracks bypass the particles and propagate through the matrix, the pores or along the particle-matrix interface and 2) above this limit, the cracks may penetrate also into the particles from the matrix or interface.

The particle-damage limit is a consequence of the combined influence of the matrix volume fraction and particle-matrix adhesion on the penetration of cracks into the particles. According to linear fracture mechanics, the

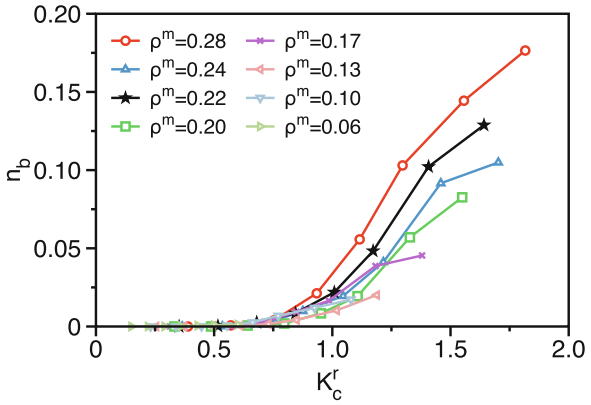

Fig. 16. Proportion n_b of broken bonds inside the particle phase as a function of the relative toughness (14) between the particle-matrix interface and the particle phase.

penetration of a crack into a particle implies that the particle is less tough than the matrix-particle interface. Otherwise, the crack will be deflected by the interface, *e.g.* [70]. For pure mode I (tensile), the toughness of any phase ϕ corresponds to the critical stress intensity factor $K_c^\phi = \sqrt{E^{[\phi]} G_c^\phi}$ and combines the effective Young's modulus $E^{[\phi]}$ with the critical energy release rate G_c^ϕ. The stored elastic energy of a bond at failure is fully dissipated when the bond fails and G_c^ϕ reads locally

$$G_c^\phi = \frac{a}{2} \frac{(\sigma^\phi)^2}{E^\phi} . \tag{11}$$

Following [8], we define the relative interface/particle toughness $K_c^r = K_c^{pm}/K_c^p$ that reads (definition of K_c^ϕ and eq. (11))

$$K_c^r = \sqrt{\frac{E^{[pm]}}{E^{[p]}} \frac{E^p}{E^{pm}}} \frac{\sigma^{pm}}{\sigma^p} . \tag{12}$$

In order to derive various estimates for this relative interface/particle toughness, the effective Young's modulus $E^{[pm]}$ of the particle-matrix interface is replaced in (12) by Young's modulus of a reference medium E^0.

A first simple choice for E^0 corresponds to a weakest link approach setting the effective ratio $E^{[pm]}/E^{[p]}$ to the local ratio E^{pm}/E^p. The relative interface/particle toughness reads in this case

$$K_c^r = \frac{\sigma^{pm}}{\sigma^p} . \tag{13}$$

Anticipating in the sequel, fig. 16 shows the proportion n_b of broken bonds inside the particles as a function of K_c^r from all simulated configurations. It is remarkable that, as compared to fig. 14, the data points are much less dispersed. Moreover, the weakest link approach is associated to the configuration for which K_c^r leads to the first occurrence of broken bonds inside the particles. In fig. 16, this situation corresponds to $K_c^r \simeq 0.4$, and the lower bound $\sigma^{pm}/\sigma^p \simeq 0.4$ is in agreement with data in fig. 15.

Another choice for E^0 corresponds to an estimate of the "particle damage limit" by setting Young's modulus of the reference medium to the effective Young's modulus $E^0 = E_{\text{eff}}$

$$K_c^r = \sqrt{\frac{E_{\text{eff}}}{E^{[p]}} \frac{E^p}{E^{pm}}} \frac{\sigma^{pm}}{\sigma^p} . \tag{14}$$

In this case, fig. 16 reveals a mean critical value $K_c^r \simeq 0.7$ below which practically no particle damage occurs. This choice for the reference modulus E^0 is motivated by the fact that the elastic energy available for the propagation of a crack is stored in the whole medium. In this way, the relative toughness provides a single particle damage criterion, which combines the two parameters ρ^m (upon which depends the effective Young's modulus, see fig. 5) and σ^{pm} (involved in (14)). The particle damage limit curve displayed in fig. 15 is simply given by eq. (14) in which the K_c^r is replaced by its mean critical value $\simeq 0.7$ and ratio $E_{\text{eff}}/E^{[p]}$ by data of fig. 5. We see that this curve represents fairly the frontier of the range of ρ^m and σ^{pm} for particle damage.

7 Conclusion

In this paper, a 3D lattice element approach was introduced for modeling cemented granular aggregates. This approach, by representing a solid material with a network of bonds connecting material points, is appropriate for the simulation of the deformation and rupture of aggregates composed of a relatively large number of particles and a binding matrix that fills partially the pore space. The stiffness and tensile strength of each bulk phase and the interface zones between different phases may be adjusted, and cracks are generated naturally as a result of breaking bonds. The mean-field mechanical model is obviously well adapted to elastic brittle behavior but it can be complexified and adapted to other behaviors. The precision may be improved by increasing the spatial resolution. In granular aggregates, composed of a dense packing of particles, it is essential to represent each particle by a large number of degrees of freedom as the structure of the packing controls to a large extent the stress transmission, and the interface with the binding matrix is a major factor for adherence between the particles and the matrix. The effect of spatial resolution was more specifically investigated in this paper with respect to the effective elastic behavior.

For a given packing fraction in all simulations, we investigated in some detail the joint effects of the matrix volume fraction and particle-matrix adhesion on the effective stiffness, global tensile strength and crack propagation. Interestingly, the effective stiffness is found to be a linear function of the matrix volume fraction in spite of the complex morphology of the matrix phase, distributed in the interstitial space of the packing. The tensile strength is an increasing function of both the matrix volume fraction and particle-matrix adhesion. Increasing the matrix volume enhances the tensile strength by increasing the adhesive surface between the matrix and particles, on one

hand, and by allowing for load transfer between the particles and the matrix and therefore a more homogeneous transmission of stresses across the aggregate.

The failure of aggregates by crack propagation in cemented aggregates is a complex process. Depending on the matrix volume fraction and particle-matrix adhesion, the cracks initiated in the matrix or particle-matrix interface may penetrate into the particles or be deflected to the interfacial zone. We showed that particle damage is controlled by the relative toughness of the interface with respect to the particles. Below a critical relative toughness, the cracks propagate only in the matrix phase or along its interface with the particles. The structure of the fracture surface as a function of different parameters including the particle size distribution is an important aspect of cemented aggregates, which was investigated in detail but will be reported later. In the same way, the influence of the packing fraction and the protocol of matrix distribution need to be analyzed for a better characterization of the aggregates.

Most properties of 3D aggregates analyzed in this paper are consistent with those reported previously for a 2D geometry as a consequence of the brittle behavior and granular disorder. The 3D aggregates appear to be more inhomogeneous due to both the linear structure of stress chains in a 3D space and the distribution of the binding material, which covers only partially the particles unless when the interstitial space is saturated by the matrix. It should be noted that, in contrast to the pore space in a 3D packing, the pores in a dense 2D packing are not contiguous. For this reason, stress transmission in 2D is always mediated by the particle phase whereas in 3D a matrix phase percolating inside the interstitial space may partially overtake independently the applied load. These aspects and the role of the percolation of the matrix may be studied only in a 3D configuration by varying the relative stiffness and strength between the matrix and particle phase.

Appendix A. Lattice element method

Lattice-type discretization has been extensively used for the statistical mechanics of fracture in disordered media, and applied to study the fracture properties of concrete and ceramics [17, 43, 46–51, 53, 54, 71]. The space is discretized as a regular or disordered grid of points (nodes) interconnected by one-dimensional elements (bonds). We used a 3D irregular meshing of the space in tetrahedral elements as shown in fig. 1. Each bond can transfer normal force, shear force and bending moment up to a threshold in force or energy. Various behaviors such as elasticity can be carried by these material lattice bonds, in contrast to the finite element approach where the local behavior is carried by volume elements.

A granular aggregate is composed of three bulk phases: particles, matrix and voids; see fig. 1. There are also two interface phases: particle-particle and particle-matrix. All elements belonging to a phase carry the same properties with a distribution that represents the intrinsic inhomogeneity of that phase. We use linear elastic-brittle elements, each element characterized by a Hooke constant and a breaking force threshold. The bonds transmit only normal forces between the lattice nodes and thus the strength of the lattice in shear and distortion is ensured only by the high connectivity of the nodes. The use of beam-like elements leads to a more realistic behavior of crack propagation for shear and distortion of the lattice, but requires considerably more computation time [43].

A sample is defined by its contour and the configuration of the phases in space. The samples are deformed by imposing displacements or forces to nodes belonging to the contour. The initial state is the reference (unstressed) configuration. The total elastic energy of the system is a convex function of node displacements and thus finding the unique equilibrium configuration of the nodes amounts to a minimization problem. Performing this minimization for stepwise loading corresponds to subjecting the system to a quasistatic deformation process. The overloaded elements (exceeding a threshold) are removed according to a breaking rule. This corresponds to irreversible micro-cracking of the lattice. If necessary, a healing mechanism can be implemented as well by restoring the broken elements. The released elastic energy between two successive equilibrium states is fully dissipated by micro-cracking.

In principle, the strain increment should be small enough in order to have only one critical bond at a time. But this method is hardly feasible, and for a reasonable choice of the strain increment, several elements may become critical (overloaded) simultaneously. Two possible rules for removing these critical elements are:

– Only the most critical bond is removed.
– All critical bonds are removed.

A breaking probability as a function of the degree of criticality may also be used [44, 47, 49, 72–74]. In order to optimize the computational effort, we adopt the second solution but with post-relaxation cycles until an equilibrium state is reached before applying the next strain increment. This gives rise to the possibility of crack propagation within one time step. Physically, this corresponds to fast unstable growth of the micro-cracks compared to the imposed strain rate.

The computational effort in solving the set of $3N$ equations by minimizing the potential energy varies in general as N^2. Since in our case N will be huge ($\simeq 3 \times 10^5$ for parametric studies), an important aspect of the algorithm is that its storage requirement should vary only linearly with N. Fortunately in our case, due to the simple additivity of the potential energy, the effort does not grow with N at all. Therefore the computation time should also depend only linearly on N.

Appendix B. Effective stiffness of a 3D periodic lattice

The effective elastic properties of a 3D periodic lattice are here derived for two standard cases: i) an elementary pat-

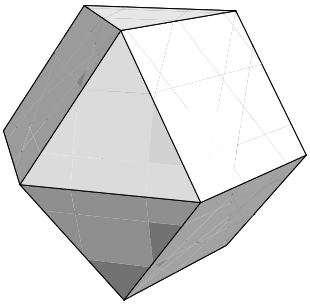

Fig. 17. A triangular orthobicupola lattice.

tern corresponding to a triangular orthobicupola (sometimes referred as the Johnson's solid #27, see fig. 17), and ii) a lattice with random orientations. These two situations correspond to overall transversely isotropic media and to isotropic media, respectively.

Denoting by $\boldsymbol{n}$ the unit vector along the transverse isotropy axis and by $\boldsymbol{i}$ the second-order identity tensor, the second-order identity tensor in the transverse plane reads $\boldsymbol{i}_T = \boldsymbol{i} - \boldsymbol{n}\otimes\boldsymbol{n}$, where $\otimes$ denotes the dyadic product. The generic basis of the fourth-order transversely isotropic and symmetric tensors is thus defined by the six following tensors:

$$\boldsymbol{E}_l = \boldsymbol{n}\otimes\boldsymbol{n}\otimes\boldsymbol{n}\otimes\boldsymbol{n}, \quad \boldsymbol{J}_t = (1/2)\boldsymbol{i}_T\otimes\boldsymbol{i}_T,$$
$$\boldsymbol{K}_t = \boldsymbol{I}_t - \boldsymbol{J}_t, \quad \boldsymbol{F} = (1/\sqrt{2})\boldsymbol{i}_T\otimes\boldsymbol{n}\otimes\boldsymbol{n}, \quad {}^{\mathsf{T}}\boldsymbol{F},$$
$$\boldsymbol{K}_l = \boldsymbol{K} - \boldsymbol{K}_t - (1/6)(2\boldsymbol{n}\otimes\boldsymbol{n} - \boldsymbol{i}_T)\otimes(2\boldsymbol{n}\otimes\boldsymbol{n} - \boldsymbol{i}_T),$$

where $\boldsymbol{I}_t$ is the fourth-order identity tensor in the transverse plane and $\boldsymbol{K} = \boldsymbol{I} - \boldsymbol{J}$ with $2\boldsymbol{I}_{ijkl} = (\boldsymbol{i}_{ik}\boldsymbol{i}_{jl} + \boldsymbol{i}_{il}\boldsymbol{i}_{jk})$ and $3\boldsymbol{J} = \boldsymbol{i}\otimes\boldsymbol{i}$, $\boldsymbol{i}$ being the second-order identity tensor. Moreover, the symmetric tensors $\boldsymbol{J}$ and $\boldsymbol{K}$ define the generic basis of the fourth-order isotropic symmetric tensors.

The effective elastic fourth-order stiffness tensor $\boldsymbol{C}$ of case i) satisfies

$$\mathcal{E}_p = \frac{1}{2}\varepsilon : \boldsymbol{C} : \varepsilon = \frac{1}{|V|}\sum_{i=1}^{12}\mathcal{E}_p^i(x_i),$$

where $\mathcal{E}_p$ and $|V| = 2\sqrt{5}/3$ are the potential energy and volume of the considered triangular orthobicupola lattice, respectively, ε is the two-order symmetric strain tensor, $\mathcal{E}_p^i(x_i) = \frac{k(x_i\cdot\varepsilon\cdot x_i)^2}{2x_i\cdot x_i}$ is the potential energy of the i-th node of the lattice with coordinates x_i, k is the Hooke constant of the lattice. For this specific lattice, one obtains after some algebra

$$\frac{\boldsymbol{C}^{(i)}}{k} = \frac{4\sqrt{2}\boldsymbol{E}_l}{5} + \frac{2(\boldsymbol{F} + {}^{\mathsf{T}}\boldsymbol{F})}{5} + \frac{2\boldsymbol{J}_t + \boldsymbol{K}_t}{\sqrt{2}} + \frac{2\sqrt{2}\boldsymbol{K}_l}{5}.$$

Following [62], the corresponding stiffness tensor for the random lattice (case ii)), is obtained by projection of the previous quantity onto the basis of the fourth-order isotropic symmetric tensors

$$\boldsymbol{C}^{(ii)} = \frac{\boldsymbol{J} :: \boldsymbol{C}^{(i)}}{\boldsymbol{J} :: \boldsymbol{J}}\boldsymbol{J} + \frac{\boldsymbol{K} :: \boldsymbol{C}^{(i)}}{\boldsymbol{K} :: \boldsymbol{K}}\boldsymbol{K} = 3\kappa^{(ii)}\boldsymbol{J} + 2\mu^{(ii)}\boldsymbol{K},$$

where the bulk modulus $\kappa^{(ii)}$ and the shear modulus $\mu^{(ii)}$ read after calculations

$$\kappa^{(ii)} = \frac{2\sqrt{2}}{5}k, \quad \mu^{(ii)} = \frac{6\sqrt{2}}{25}k.$$

The corresponding Young's modulus and Poisson ratio are thus

$$E = \frac{9\kappa^{(ii)}\mu^{(ii)}}{3\kappa^{(ii)} + \mu^{(ii)}} = \frac{3\sqrt{2}}{5}k, \quad \nu = \frac{3\kappa^{(ii)} - 2\mu^{(ii)}}{2(3\kappa^{(ii)} + \mu^{(ii)})} = \frac{1}{4}.$$

We assume in this paper that this type of constraint on the Poisson ratio does not have a strong influence on the crack regimes of cemented granular aggregates.

Appendix C. Node stresses

The definition of the Cauchy stress tensor assumes a sufficiently large number of material points inside a control volume so that the surface density of forces is statistically well defined. Following a general framework first introduced by Moreau, one can attribute a stress tensor to each node [58,75]. The physical content of this tensor remains the same whether applied to a node or to a portion of space including several nodes, and it tends to the Cauchy stress tensor at large scales.

In the framework of the virtual power formalism, a force (in the general sense) experienced by a bounded portion S of a material system is defined through the expression of the power $\mathcal{P}$ that it develops when subjected to a virtual velocity field $\boldsymbol{v}(\boldsymbol{r})$. Let $\boldsymbol{v}(\boldsymbol{r})$ be an affine field,

$$v_\alpha(\boldsymbol{r}) = v_\alpha(0) + b_{\alpha\beta}r_\beta, \tag{C.1}$$

where we assume Einstein's summation rule over subscripts. By definition, the power $\mathcal{P}_{\text{int}}(\boldsymbol{v})$ of internal forces is linear in $\boldsymbol{v}$. This means that there exist $\boldsymbol{R}$ and $\boldsymbol{M}$ such that

$$\mathcal{P}_{\text{int}} = R_\alpha v_\alpha(0) + M_{\alpha\beta}b_{\alpha\beta}. \tag{C.2}$$

In the particular case of a rigid body motion, $\boldsymbol{b}$ is antisymmetric ($b_{\alpha\beta} = -b_{\beta\alpha}$) and $\mathcal{P}_{\text{int}} = 0$ by virtue of Newton's third law. This implies that $\boldsymbol{R} = 0$ and $\boldsymbol{M}$ is a symmetric tensor of rank 2 and independent of the choice of the reference frame. Following Moreau, we will refer to $\boldsymbol{M}$ as the internal moment tensor of the volume S [58].

The internal moment tensor can be evaluated without restriction for any portion S of the system. In particular, we tesselate the space by Voronoi cells whose faces are bisectors of the segments joining the nodes, fig. 2. The internal moment of a cell i (centered on node i) can then be calculated by assuming force balance at each node. The total power $\mathcal{P} = \mathcal{P}_{\text{int}} + \mathcal{P}_{\text{ext}}$, where $\mathcal{P}_{\text{ext}}$ is the power associated with external forces, is zero irrespective of the

choice of virtual velocities. Since the only forces $\boldsymbol{f}^{ij}$ acting on the node i are exerted at the midpoints $\boldsymbol{r}^{ij}$ of the bonds ij by neighboring nodes j, the internal power is given by $\mathcal{P}_{\text{int}}(p) = -\mathcal{P}_{\text{ext}}(p) = -\sum_j v_\alpha(\boldsymbol{r}^{ij}) f_\alpha^{ij}$. Identifying this with the general expression (C.2) of the internal power, yields

$$M_{\alpha\beta}(i) = -\sum_j r_\alpha^{ij} f_\beta^{ij}. \tag{C.3}$$

It can be shown that this expression holds also in the presence of bulk forces (gravity) acting at the lattice nodes if the origin of coordinates for each cell is placed at its center.

The internal moment $\boldsymbol{M}^{i\cup j}$ of two nodes i and j sharing the bond ij is the sum of their respective internal moments $\boldsymbol{M}^i$ and $\boldsymbol{M}^j$ because opposite reaction forces of equal magnitude act on the two nodes at the same midpoint. This additive property implies that the total internal moment $\boldsymbol{M}(S)$ of a portion S of space is simply the sum of the internal moments of all nodes belonging to S. On the other hand, if the number of nodes in S is sufficiently large, it makes sense to evaluate the Cauchy stress tensor $\boldsymbol{\sigma}$ for S. Assuming the same test field as (C.1), the corresponding internal power by definition of $\boldsymbol{\sigma}$ is

$$\mathcal{P}_{\text{int}} = \int_S \sigma_{\alpha\beta}\partial_\alpha v_\beta \mathrm{d}V. \tag{C.4}$$

Then, according to (C.2), we have

$$M_{\alpha\beta}(S) = \int_S \sigma_{\alpha\beta}\mathrm{d}V = \langle\sigma_{\alpha\beta}\rangle V. \tag{C.5}$$

This shows that the internal moment tensor of S per unit volume ($\boldsymbol{M}/V$) tends to the average Cauchy stress tensor $\langle\sigma_{\alpha\beta}\rangle$ at larger scales or for an increasing number of nodes contained in S.

We see that the internal moment tensor per unit volume in a discrete system plays the same role as the Cauchy stress tensor in a continuous medium. For this reason, it is legitimate to define "node stresses" $\sigma_{\alpha\beta}(i)$ by simply dividing the internal moment of the nodes by the volume $V(i)$ of the corresponding Voronoi cells

$$\sigma_{\alpha\beta}^i = \frac{1}{V^i}\sum_j r_\alpha^{ij} f_\beta^{ij}. \tag{C.6}$$

Appendix D. Estimates of elastic behaviors

The effective elastic properties of porous cemented granular aggregates (as depicted in fig. 1) can be estimated with the help of two scale transitions.

The first scale concerns the "interphase" between the particles (see fig. 18). This interphase, denoted by *iph*, is composed of particle-particle interface (fourth-order stiffness tensor $\boldsymbol{C}^{[pp]}$, volume fraction ρ^{pp}) inserted within a ring of matrix (stiffness tensor $\boldsymbol{C}^{[m]}$, volume fraction ρ^m). The effective elastic properties of this interphase can be deduced from the Voigt bound (the relative volume fractions of the particle-particle interface and of the matrix in this composite are $\rho^{pp}/(\rho^{pp}+\rho^m)$ and $\rho^m/(\rho^{pp}+\rho^m)$ respectively)

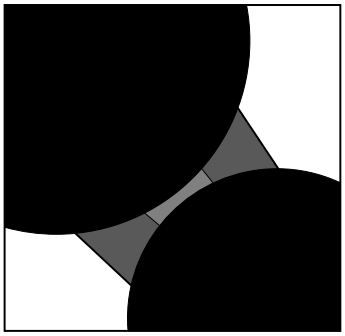

Fig. 18. Sketch of porous cemented granular composite. Three main phases: particles (black), pores (white), interphase (particle-particle interface in light gray + matrix in gray). The matrix-particle interface is associated to the matrix pahse.

$$\boldsymbol{C}^{[iph]} = \frac{\rho^m}{\rho^{pp}+\rho^m}\boldsymbol{C}^{[m]} + \frac{\rho^{pp}}{\rho^{pp}+\rho^m}\boldsymbol{C}^{[pp]}.$$

The second scale transition concerns a three-phase composite: particles (stiffness tensor $\boldsymbol{C}^{[p]}$, volume fraction ρ^p), voids (vanishing stiffness tensor, volume fraction ρ^v), interphase defined in the first scale transition (stiffness tensor $\boldsymbol{C}^{[iph]}$, volume fraction $\rho^{iph} = 1-\rho^p-\rho^v$). As a first approximation, each phase is considered as spherical in shape and randomly distributed in space. The effective elastic properties $\boldsymbol{C}_{\text{eff}}$ of this composite is thus estimated with the help of the Hashin-Shtikman's result [36]

$$\begin{aligned}\left(\boldsymbol{C}_{\text{eff}} + \boldsymbol{C}^*(\boldsymbol{C}^0)\right)^{-1} = {}& \rho^p\left(\boldsymbol{C}^{[p]} + \boldsymbol{C}^*(\boldsymbol{C}^0)\right)^{-1} \\ & + \rho^{iph}\left(\boldsymbol{C}^{[iph]} + \boldsymbol{C}^*(\boldsymbol{C}^0)\right)^{-1} \\ & + \rho^v \boldsymbol{C}^*(\boldsymbol{C}^0)^{-1},\end{aligned} \tag{D.1}$$

where $\boldsymbol{C}^*(\boldsymbol{C}^0)$ is the Hill influence tensor associated to the fourth-order stiffness tensor $\boldsymbol{C}^0$ of a reference medium. For a random distribution of phases, this influence tensor reads

$$\boldsymbol{C}^*(\boldsymbol{C}^0) = 4\mu^0\boldsymbol{J} + \frac{\mu^0(9\kappa^0+8\mu^0)}{3(\kappa^0+\mu^0)}\boldsymbol{K},$$

where κ^0 and μ^0 are the bulk and the shear moduli of the reference medium respectively.

Since the considered microstructure exhibits overall isotropy, eq. (D.1) allows to derive the effective bulk modulus κ_{eff} and the effective shear modulus μ_{eff} as $\boldsymbol{C}_{\text{eff}} = 3\kappa_{\text{eff}}\boldsymbol{J} + 2\mu_{\text{eff}}\boldsymbol{K}$, and the effective Young's modulus is thus obtain as

$$E_{\text{eff}} = \frac{9\kappa_{\text{eff}}\mu_{\text{eff}}}{3\kappa_{\text{eff}}+\mu_{\text{eff}}}.$$

The estimates drawn in fig. 5 are straightforward:

– the effective initial Young's modulus with bare contacts between particles ($\sigma^{pp} = 0$) corresponds to a vanishing stiffness for the particle-particle interface and a reference medium set as the interphase

$$\boldsymbol{C}^{[pp]} = 0, \quad \boldsymbol{C}^0 = \boldsymbol{C}^{[iph]} \quad \text{for bare contacts;}$$

– the effective initial Young's modulus with adhesive contacts ($\sigma^{pp} = \sigma^{pm}$) corresponds to a particle-particle interface set as particle-matrix interface and to a reference medium set as particule

$$\boldsymbol{C}^{[pp]} = \boldsymbol{C}^{[pm]}, \quad \boldsymbol{C}^0 = \boldsymbol{C}^{[p]} \quad \text{for adhesive contacts.}$$

References

1. E.J. Tarbuck, F.K. Lutgens, *Earth – An introduction to Physical Geology* (Pearson Education, New Jersey, 2005).
2. I.J. Merchant, D.E. Macphee, H.W. Chandler, R.J. Henderson, Cement Concrete Res. **31**, 1873 (2001).
3. E. Schlangen, J.G.M. Van Mier, Cement Concrete Comp. **14**, 105 (1992).
4. F. de Larrard, A. Belloc, ACI Mater. J. **94**, 417 (1997).
5. A. Benhamida, F. Bouchelaghem, H. Dumontet, Int. J. Numer. Analy. Methods Geomech. **29**, 187 (2005).
6. Y. Pomeranz, *Wheat: Chemistry and technology* (AACC, St Paul USA, 1988).
7. W. Atwell, *Wheat Flour* (AACC, St Paul USA, 2001).
8. V. Topin, J.Y. Delenne, F. Radjai, L. Brendel, F. Mabille, Eur. Phys. J. E **23**, 413 (2007).
9. K. Johnson, K. Kendall, A. Roberts, Proc. R. Soc. London, Ser. A (Math. Phys. Sci.) **324**, 301 (1971).
10. K. Kendall, N. Alford, J. Birchall, British Ceramic Proc. **37**, 255 (1986).
11. K. Johnson, *Contact Mechanics* (Cambridge University Press, Cambridge, 1999).
12. A. Castellanos, Adv. Phys. **54**, 263 (2005).
13. D. Elata, J. Dvorkin, Mech. Mater. **23**, 147 (1996).
14. F. Sienkiewicz, A. Shukla, M. Sadd, Z. Zhang, J. Dvorkin, Mech. Mater. **22**, 43 (1996).
15. L. Zhonghua, S. Schmauder, Comput. Mater. Sci. **18**, 295 (2000).
16. O. Buyukozturk, B. Hearing, Int. J. Solids Struct. **35**, 4055 (1998).
17. G. Lilliu, J.G.M. Van Mier, Engin. Fract. Mech. **70**, 927 (2003).
18. H. Tan, Y. Huang, C. Liu, P. Geubelle, Int. J. Plasticity **21**, 1890 (2005).
19. F. de Larrard, *Concrete mixture proportioning. A scientific approach* (E & FN SPON, London, 1991).
20. Z. Hashin, P.J.M. Monteiro, Cement Concrete Res. **32**, 1291 (2002).
21. P.A. Cundall, O.D.L. Strack, Géotechnique **29**, 47 (1979).
22. C. Thornton, C.W. Randall, *Applications of theoretical contact mechanics to solid particle system simulation*, in *Micromechanics of granular media* (Elsevier, Amsterdam, 1988).
23. J. Moreau, Eur. J. Mech. A/Solids **13**, 93 (1994).
24. H.G. Matuttis, S. Luding, H.J. Herrmann, Powder Technol. **109**, 278 (2000).
25. T. Pöschel, T. Schwager, *Computational granular dynamics: models and algorithms* (Springer, Berlin, 2005).
26. F. Radjai, F. Dubois (Editors), *Discrete-element Modeling of Granular Materials* (Iste-Wiley, London, 2011).
27. S. Roux, *Quasi-static contacts*, in *Physics of Dry Granular Media*, edited by H.J. Herrmann, J.P. Hovi, S. Luding (Kluwer Academic Publishers, Dordrecht, 1998), p. 267.
28. S. Luding, *Collisions and Contacts between two particles*, in *Physics of dry granular media, NATO ASI Ser. E350*, edited by H.J. Herrmann, J.P. Hovi, S. Luding (Kluwer Academic Publishers, Dordrecht, 1998), p. 285.
29. F. Radjai, I. Preechawuttipong, R. Peyroux, *Cohesive granular texture*, in *Continuous and discontinuous modelling of cohesive frictional materials*, edited by P. Vermeer, S. Diebels, W. Ehlers, H. Herrmann, S. Luding, E. Ramm (Springer Verlag, Berlin, 2001), pp. 148–159.
30. J.Y. Delenne, V. Topin, V. Richefeu, F. Dubois, F. Radjai, *Discrete-element modeling of granular materials* (Iste-Wiley, London, 2011), chapt. Numerical modeling of cohesive interactions, pp. 263–302.
31. F. Kun, H. Carmona, J. Andrade, H. Herrmann, Phys. Rev. Lett. **100**, 094301 (2008).
32. H.A. Carmona, F.K. Wittel, F. Kun, H. Herrmann, Phys. Rev. E **77**, 051302 (2008).
33. F. Kun, H.J. Herrmann, Phys. Rev. E **59**, 2623 (1999).
34. H. Carmona, F. Kun, J. Andrade, H. Herrmann, Phys. Rev. E **75**, 046115 (2007).
35. F.K.G. Timar, J. Blomer, H.J. Herrmann, Phys. Rev. Lett. **104**, 095502 (2010).
36. Z. Hashin, S. Shtrikman, J. Mech. Phys. Solids **11**, 127 (1963).
37. J. Halpin, S. Tsai, *Environmental factors estimation in composite materials design*, Air Force Materials Lab. Technical report, AFML-TR-67-423 (1967).
38. J. Eshelby, Proc. R. Soc. London **241**, 376 (1957).
39. G.I. Barenblatt, Adv. Appl. Mech. **7**, 55 (1962).
40. Z. Wang, L. Ma, L. Wu, H. Yu, Acta Mech. Solida Sinica **25**, 9 (2012), ISSN 0894-9166.
41. A. Ayyar, N. Chawla, Compos. Sci. Technol. **66**, 1980 (2006).
42. S. Roux, H.J. Herrmann, *Statistical Models for Fracture in Disordered Media* (North Holland, Amsterdam, 1990), chap. Continuum and discrete description of elasticity and other rheological behavior, pp. 87–114.
43. E. Schlangen, E.J. Garboczi, Engin. Fract. Mech. **57**, 319 (1997).
44. G.M.J. VanMier, M.B. Chiaia, A. Vervuurt, Comput. Methods Appl. Mech. Engin. **142**, 189 (1997).
45. C. Chang, T. Wang, L. Sluys, J.V. Mier, Engin. Fract. Mech. **69**, 1959 (2002).
46. B. Chiaia, A. Vervuurt, J.G.M. Van Mier, Engin. Fract. Mech. **57**, 301 (1997).
47. A. Delaplace, G. Pijaudier-Cabot, S. Roux, J. Mech. Phys. Solids **44**, 99 (1996).
48. S. Feng, M.F. Thorpe, E. Garboczi, Phys. Rev. B **31**, 276 (1985).
49. H.J. Herrmann, S. Roux, *Statistical Models for Fracture in Disordered Media* (North Holland, Amsterdam, 1990).
50. H. Gao, P. Klein, J. Mech. Phys. Solids **46**, 187 (1998).
51. E.P. Prado, J.G.M. van Mier, Engin. Fract. Mech. **70**, 1793 (2003).
52. J.G.M. VanMier, M.R.A. van Vliet, T.K. Wang, Mech. Mater. **34**, 705 (2002).
53. H.J. Vogel, H. Hoffmann, A. Leopold, K. Roth, Geoderma **125**, 213 (2005).

54. H.J. Vogel, H. Hoffmann, K. Roth, Geoderma **125**, 203 (2005).
55. J. Delenne, V. Topin, F. Radjai, Acta Mech. **205**, 9 (2009), ISSN 0001-5970.
56. J.G.M. VanMier, M.R.A. van Vliet, Construct. Build. Mater. **13**, 3 (1999).
57. V. Topin, F. Radjai, J.Y. Delenne, A. Sadoudi, F. Mabille, J. Cereal Sci. **47**, 347 (2007).
58. J.J. Moreau, *Numerical Investigation of Shear Zones in Granular Materials*, in *Friction, Arching, Contact Dynamics*, edited by D.E. Wolf, P. Grassberger (World Scientific, Singapore, 1997), pp. 233–247.
59. V. Topin, F. Radjai, J.Y. Delenne, F. Mabille, Powder Technol. **190**, 215 (2009), ISSN 0032-5910.
60. L. Dormieux, D. Kondo, F.J. Ulm (Editors), *Microporomechanics* (Wiley, England, 2006).
61. A. Roberts, M. Teubner, Phys. Rev. E **51**, 4141 (1995).
62. J.M. Gatt, Y. Monerie, D. Laux, D. Baron, **336**, 11 (2005).
63. F. Radjai, D.E. Wolf, M. Jean, J. Moreau, Phys. Rev. Lett. **80**, 61 (1998).
64. C. Liu, S.R. Nagel, D.A. Schecter, S.N. Coppersmith, S. Majumdar, O. Narayan, T.A. Witten, Science **269**, 513 (1995).
65. F. Radjai, M. Jean, J. Moreau, S. Roux, Phys. Rev. Lett. **77**, 274 (1996).
66. L.E. Silbert, G.S. Grest, J.W. Landry, Phys. Rev. E **66**, 1 (2002).
67. V. Richefeu, F. Radjai, M. El Youssoufi, Eur. Phys. J. E **21**, 359 (2006).
68. F. Radjai, D.E. Wolf, Granular Matter **1**, 3 (1998).
69. L. Dormieux, E. Lemarchand, D. Kondo, E. Fairbairn, Mater. Struct. **37**, 31 (2004).
70. M.Y. He, J.W. Hutchinson, Int. J. Solids Struct. **25**, 1053 (1989).
71. C.S. Chang, T.K. Wang, L.J. Sluys, J.G.M. van Mier, Engin. Fract. Mech. **69**, 1941 (2002).
72. J. Fitoussi, G. Guo, D. Baptiste, Comp. Sci. Technol. **58**, 759 (1998).
73. G.K. Hu, G. Guo, D. Baptiste, Comput. Mater. Sci. **9**, 420 (1998).
74. L. Mishnaevsky Jr., K. Derrien, D. Baptiste, Compos. Sci. Technol. **64**, 1805 (2004).
75. L. Staron, F. Radjai, J.P. Vilotte, Eur. Phys. J. E **18**, 311 (2005).